Oscillations of low-current electrical discharges between parallel-plane electrodes. III. Models

A. V. Phelps,* Z. Lj. Petrović,† and B. M. Jelenković†
Joint Institute for Laboratory Astrophysics, University of Colorado and National Institute of Standards and Technology, Boulder, Colorado 80309-0440
(Received 29 October 1992)

Simple models are developed to describe the results of measurements of the oscillatory and negative differential resistance properties of low- to moderate-current discharges in parallel-plane geometry. The time-dependent model assumes that the ion transit time is fixed and is short compared to the times of interest, that electrons are produced at the cathode only by ions, and that space-charge distortion of the electric field is small but not negligible. Illustrative numerical solutions are given for large voltage and current changes and analytic solutions for the time dependence of current and voltage are obtained in the small-signal limit. The small-signal results include the frequency and damping constants for decaying oscillations following a voltage change or following the injection of photoelectrons. The conditions for underdamped, overdamped, and self-sustained or growing oscillations are obtained. A previously developed steady-state, nonequilibrium model for low-pressure hydrogen discharges that includes the effects of space-charge distortion of the electric field on the yield of electrons at the cathode is used to obtain the negative differential resistance. Analytic expressions for the differential resistance and capacitance are developed using the steady-state, local-equilibrium model for electron and ion motion and a first-order perturbation treatment of space-charge electric fields. These models generally show good agreement with data from dc and pulsed discharge experiments presented in the accompanying papers.

PACS number(s): 52.80.Dy, 52.80.Hc, 52.40.Hf

I. INTRODUCTION

In this paper we develop simple models of the oscillatory and negative differential resistance behavior of low-current electrical discharges needed to describe the experimental results obtained in the previous two papers [1,2]. A number of authors [3–15] have discussed models of the response of low-pressure parallel-plate discharges at low currents and at moderate currents to small alternating voltages superimposed on the dc voltage used to maintain the discharge. Particularly useful is the extensive unpublished review by Ecker and Müller [15].

The second topic of this paper is the extension of models for the effects of space-charge distortion on breakdown [15–19] to the calculation of the differential resistance of low-current discharges [9,18,19]. This negative resistance plays a crucial role in the theory of the observed instabilities and oscillations [3–5,9,15]. We show that the differential capacitance caused by space charge can be neglected for our conditions.

The ability to model the cathode regions of electrical discharges in gases has increased dramatically in recent years because of the availability of high-speed, large-memory computers capable of handling the equations and data describing the very complex combination of physical processes occurring in these discharges [6,8,20,21]. Motivation for such modeling has been provided by the application of low-pressure discharges to plasma processing [20–22], switches [23], and lasers [24].

We first develop a model of transient current and voltage behavior based on an extension of the conventional equilibrium model of electron and ion motion. This model contains three phenomenological constants, i.e., the effective ion-induced electron emission yield, the effective ion transit time, and the negative differential resistence. The model is found to work well for low currents at both moderate E/n, where equilibrium applies to electron and ion motion, and at very high E/n, where nonequilibrium effects are dominant (here E/n is the ratio of the electric field E to the gas density n). Secondly, the phenomenological constants are related to the electron and ion transport coefficients and the ion-induced yield of electrons at the cathode appropriate to the equilibrium model. The equilibrium model and the numerical nonequilibrium model yield current growth coefficients and negative differential resistances in approximate agreement with experiment.

The experiments to which the models apply are summarized in Sec. II. A simple theory of the discharge oscillations is developed and applied in Sec. III. A steady-state model of space-charge distortion of the electric field and its effects on the differential resistance and capacitance is presented in Sec. IV. The results of the theory are also compared with experiment in the accompanying papers [1,2], hereafter referred to as papers I and II.

II. SUMMARY OF EXPERIMENT

Figure 1 shows a schematic of the discharge tube and associated circuitry used in measurements of the properties of low-current, low-pressure discharges in parallel-plane geometry [1,2]. Dimensions for the parallel-plane electrodes for the experiments of I and II are 7.8 cm in diameter (area 50 cm^2) with a separation of 1.05 cm. The gas pressures are from 40 to 400 Pa (0.3 to 3 Torr) and the discharge current densities range from $<10^{-7}$ to 2

 ©1993 The American Physical Society

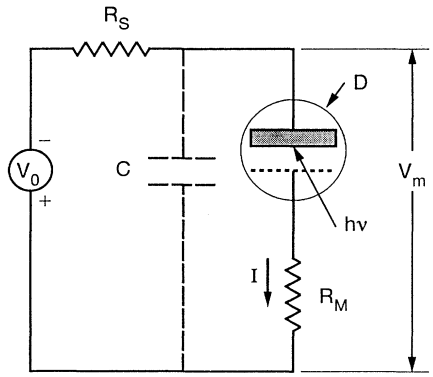

FIG. 1. Schematic of idealized discharge tube and electrical circuit modeled in this paper.

mA/cm^2.

The experimental results to be modeled are (i) the frequencies and damping constants of the decaying oscillations in current and voltage resulting when either a pulse of photoelectrons is released from the cathode (paper I) or a pulse of voltage is applied to a circuit (paper II); (ii) the limits of self-sustained oscillations as discussed in paper I and growing oscillations appropriate to paper II; (iii) the transient current following the application of a voltage pulse to the circuit from paper II; and (iv) the negative resistance behavior of the steady-state, voltage-current characteristic as measured in paper II.

III. MODEL OF TRANSIENTS IN LOW-CURRENT DISCHARGES

The model developed in this section is intended to describe the transient current and voltage, including damped oscillations, resulting when either a pulse of photoelectrons is released from the cathode or a pulse of voltage is applied to the discharge circuit. It will also be used to investigate the circuit and discharge parameters that determine the limits for self-sustained or growing oscillations and to calculate the associated current and voltage wave forms. We assume the following.

(i) Space-charge distortion of the electric field over our range of currents is small enough so that its effects can be represented by a negative differential resistance.

(ii) The times for significant changes in the electric field and current are long compared to the electron and ion transient times.

(iii) Electrons are produced at the cathode only by ions. Electron production by fast atoms is included in the ion contribution. Electron production by photon arrival at the cathode is assumed to be small. Similarly, electron production by metastables is assumed small.

(iv) The round-trip electron number gain g resulting from an electron released from the cathode is a unique function of the nd and V values for the discharge. Here n is the gas density, d is the separation of the parallel-plane electrodes, and V is the discharge voltage. The number gain has been thoroughly discussed for the higher-pressure discharges [6,8] and is reviewed in Ref. [22] for low-pressure, high-voltage discharges.

(v) Ionization is by electron impact only, i.e., ionization by heavy particles is neglected.

(vi) The electron multiplication is an exponential function of position with a spatial ionization coefficient of α/n that is a function of E/n. This assumption could be relaxed for quasi-steady-state low-pressure nonequilibrium discharges rather simply by replacing the exponential growth by an empirical fit to nonequilibrium calculations of the electron multiplication [25] appropriate to each E/n and nd. We have not done so.

(vii) The electron and ion currents are assumed to be uniformly distributed over the surface of the electrodes of area A, i.e., $I_x = AJ_x$, where J_x is the current density for species x. The evidence regarding discharge constrictions is reviewed in I. The effects of the small space-charge electric fields on assumptions (i) and (iii) through (iv) are discussed in Sec. IV.

With these assumptions, the electron current at the cathode $I_e(0,t+T)$ at the time $t+T$ is related to the current $I_e(0,t)$ at the time t by [4,6,13]

$$I_e(0,t+T)=I_p(0,t+T)+\gamma I_e(0,t)[e^{\alpha(t)d}-1] +\delta\gamma I_e(0,t)e^{\alpha(t)d} , \quad (1)$$

where $I_p(0,t+T)$ is the photoelectric current produced by irradiation of the cathode, T is the ion transit time and is the time between successive avalanches, γ is the effective yield of electrons per ion arriving at the cathode, and δ is the yield of ions produced by backscattered electrons per electron arriving at the anode. Here γ includes the contribution of fast neutrals. The electron current at the cathode can also be written as an expansion in time about the time t. Thus,

$$I_e(0,t+T)=I_e(0,t)+T\frac{dI_e(0,t)}{dt} . \quad (2)$$

Elimination of $I_e(0,t+T)$ gives

$$\frac{dI_e(0,t)}{dt}=\frac{I_p(0,t)}{T}+\frac{[g(t)-1]}{T}I_e(0,t) , \quad (3)$$

where the electron number gain g is given by

$$g(t)=\gamma[(1+\delta)e^{\alpha(t)d}-1] . \quad (4)$$

Beginning with Eq. (3) we have neglected the difference between $I_p(0,t+T)$ and $I_p(0,t)$ because we are not worried about the detailed time dependence of the photocurrent and are only concerned with the integrated effect of the very short pulse.

The electron current emitted from the cathode is given by

$$I_e(0,t)=\gamma I_+(0,t) , \quad (5)$$

where I_+ is the positive ion current. From

$$I=I_e+I_+ , \quad (6)$$

the total current $I(t)$ is related to the electron current $I_e(0,t)$ at the cathode by

$$\frac{I}{I_e(0,t)}=\frac{(1+\gamma)}{\gamma} . \tag{7}$$

We will assume that γ can be written as

$$\gamma=\gamma_p+k_V V+k_I I , \tag{8}$$

where the γ_p represents the "potential ejection" of electrons and is small for hydrogen ions [6,8,26], the k_V term is an approximation to the contribution of "kinetic" ejection of electrons [6,8,26], and the k_I term represents the first-order effects of space charge on the electric field and, thereby, the electron yield at the cathode. In the second term of Eq. (8) we have assumed that the yield of electrons is determined by the discharge voltage V, as would be the case for discharges where the positive ions cross the discharge under free-fall conditions. Such an assumption is appropriate for low-pressure discharges and ions that do not have large charge-transfer cross sections, e.g., H^+ in H_2. A near linear variation of yield with V is typical of electron yields at ion (and neutral atom) energies of the order of 100 eV [26]. The term proportional to I was proposed by Rogowski [16] and assumes that the energy of the ions striking the cathode is determined by the E/n at the cathode, as would be appropriate for ions with a short mean-free path for charge-transfer collisions. This term is discussed further in Secs. IV A and IV B. Our assumption that ion-induced electron emission is dominant is not expected to be valid for $E/n < 500$ Td [6,8]. Here uv photon-induced electron emission dominates and γ is roughly independent of E/n and V [6,8] for the E/n considered.

We will neglect the variation in δ with V and I for the moderately high E/n considered here, although previous models [25] have shown that for very high E/n discharges δ can increase with decreasing electric field at the anode because of increased numbers of collisions by the lower-energy backscattered electrons. We approximate α using the empirical expression for α/n versus E/n given in the Appendix [6,8,27]. For discharges in atomic gases, such as Ar, where a single ion is present, we expect the ion transit time to vary as $(E/n)^{-1}$ [28]. However, on the basis of measurements [29] of photoelectric-induced current transients in H_2, we expect the effective ion transit time in H_2 to vary slowly with V and E/n for $E/n > 500$ Td. Combining Eqs. (3), (5), and (7), we obtain

$$\frac{dI}{dt}=\frac{(1+\gamma)}{\gamma}\frac{dI_e}{dt}-\frac{I_e}{\gamma^2}\left[\frac{\partial\gamma}{\partial V}\frac{dV}{dt}+\frac{\partial\gamma}{dI}\frac{dI}{dt}\right] . \tag{9}$$

Elimination of I_e from Eqs. (3) and (9) gives an equation representing the characteristics of the discharge as

$$\frac{dI}{dt}=\left[\frac{(1+\gamma)I_p}{\gamma T}+\frac{(g-1)I}{T}-\frac{Ik_V}{\gamma(1+\gamma)}\frac{dV}{dt}\right]\times\left[1+\frac{Ik_I}{\gamma(1+\gamma)}\right]^{-1} . \tag{10}$$

The equation for the discharge voltage V in terms of the discharge current I and the circuit components shown in Fig. 1 is

$$\frac{dV(t)}{dt}=\frac{1}{R_S C}[V_0(t)-V(t)-I(t)(R_S+R_m)]-R_m\frac{dI(t)}{dt} , \tag{11}$$

where C includes the capacitance of cables and high-voltage leads as well as that of the electrodes, R_S is the series resistance, and $V_0(t)$ is the power supply voltage including any voltage pulse. The monitor resistance R_m is used to measure the discharge current. The capacitance of the electrodes [30] is sufficiently small so that we neglect the resonant circuit formed by the discharge and the electrodes. For the data of paper II, the use of an operational amplifier to measure the discharge current resulted in an effective value of $R_m=0$. The measured "total" voltage V_m is that developed across the circuit capacitance and is given by $V_m=V(t)+I(t)R_m$.

A. Numerical solutions

Numerical solutions of the transient model represented by Eqs. (10) and (11) allow for arbitrarily large changes in current and voltage. Empirical analytical fits to data, such as ionization coefficients, are used. The numerical solutions are obtained using a personal computer and a routine [31] that solves large sets of first-order differential equations with nonlinear coefficients that are continuous, piecewise-analytic functions of the dependent variables. Figure 2 shows representative calculations of the current and voltage transients. Similar comparisons of experiment and the model are also shown in Fig. 8 of I and Fig. 2 of II. Typical calculation times were several seconds on

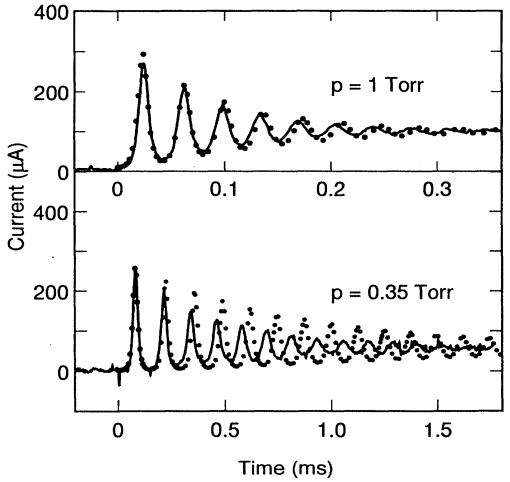

FIG. 2. Representative current transients resulting from the application of voltage pulses to parallel-plane discharges in H_2. The curves are from the experiments described in II with $C=250$ pF and $A=50$ cm^2. $R_S=10^6$ Ω and 10^5 Ω for $p=0.35$ and 1 Torr, respectively. The upper curve is for a sustaining discharge operating at $p=1$ Torr, $I(0)=10$ μA, and $V_B=345$ V, while the lower curve is for $p=0.35$ Torr, $I(0)=2$ μA, and $V_B=1025$ V. The points are the results of calculations using Eqs. (10) and (11).

a 33-MHz personal computer.

In Fig. 2 the steady-state currents I_{SS} and series resistances R_S are chosen by the experimentalist to yield a damped sine wave response to voltage pulses at the pressures of 0.35 and 1 Torr. Note that we have not plotted current densities in figures such as Fig. 2 because one cannot scale the results to other cathode areas without consideration of whether C and R_S are varied. See paper I and Sec. III C for a discussion of the limits on I_{SS} and R_S. For the calculations of Fig. 2 the amplitude of the applied voltage pulse is adjusted to produce the measured currents at late times. The only other adjustable parameter is the current in the sustaining discharge, i.e., the discharge current prior to the pulse, for the 0.35-Torr case where this current was not accurately determined. The other coefficients of the model were taken from the fits to angular frequency and current normalized inductance as described in paper II and in the Appendix.

It should be pointed out that the calculated delay in the development of the first current spike, i.e., equivalent to the "formative time lag" of conventional electrical breakdown [6,27], is particularly sensitive to parameters such as the sustaining current and the pulse voltage amplitude (see paper II, Sec. VI). Also, the discrepancy in the angular frequency in the 0.35-Torr case is $<10\%$ and is considered reasonable in view of cathode aging effects. The difference between the apparent damping and that calculated for $p=0.35$ Torr is similar to that found in papers I and II and may be an experimental problem. We consider the agreement between the model and experimental current transients to be good. Similar agreement (not shown) is found for the voltage wave forms.

B. Small-signal model

We next obtain analytic transient solutions for small changes in voltage and current about their steady-state values. Steady-state solutions appropriate for ac impedance measurements have been obtained by several authors [4,5,7,11,13–15] for high-current experiments and by Sigmond [9] for low-current experiments, such as ours. For small fractional changes in current I and voltage V

$$V(t)=V_{SS}+\beta v(t)\ , \tag{12}$$

$$I(t)=I_{SS}+\beta i(t)\ , \tag{13}$$

and

$$g(t)=1+\beta\frac{\partial g}{\partial V}v(t)+\beta\frac{\partial g}{\partial I}i(t)\ , \tag{14}$$

where β is the perturbation parameter, I_{SS} and V_{SS} are the steady-state discharge current and voltage, the lowercase i and v are the time-dependent components of the current and voltage, and

$$V_{SS}=V_0-I_{SS}(R_S+R_m)\ . \tag{15}$$

Substituting Eqs. (12) to (15) into Eqs. (10) and (11) for $I_p(t)=0$ and retaining only terms that are first order in β, we obtain

$$\left[1+\frac{I_{SS}k_I}{\gamma_{SS}(1+\gamma_{SS})}\right]\frac{di}{dt}=\frac{I_{SS}}{T}\frac{\partial g}{\partial V}v-\frac{I_{SS}k_V}{\gamma(1+\gamma)}\frac{dv}{dt}+\frac{I_{SS}k_I}{T\gamma_{SS}}i \tag{16}$$

and

$$\frac{dv}{dt}=-\frac{v}{R_SC}-\frac{i}{C}\left[1+\frac{R_m}{R_S}\right]-R_m\frac{di}{dt}\ . \tag{17}$$

Equations (16) and (17) are coupled linear first-order differential equations and are readily solved for $i(t)$ and $v(t)$. For our present purposes we need only the roots of the determinant which occurs, for example, when solving the equations using the Laplace transform technique.

At intermediate I_{SS} the roots are complex and the current $i(t)$ and voltage $v(t)$ vary as

$$i(t)=D\exp(-\kappa t)\sin(\omega t+\phi_1)\ , \tag{18}$$

and

$$v(t)=G\exp(-\kappa t)\sin(\omega t+\phi_2)\ , \tag{19}$$

where

$$\omega^2=\frac{I_{SS}}{R_SCT}\left[(R_S+R_m)\frac{\partial g}{\partial V}-\frac{k_I}{\gamma_{SS}}\right]\times\left[1+\frac{I_{SS}(k_I-R_mk_V)}{\gamma_{SS}(1+\gamma_{SS})}\right]^{-1}-\kappa^2\ , \tag{20}$$

$$\kappa=\frac{1}{2R_SC}\left[1+\frac{I_{SS}[k_I-(R_S+R_m)k_V]}{\gamma_{SS}(1+\gamma_{SS})}-\frac{R_SCI_{SS}}{T}\left[\frac{k_I}{\gamma_{SS}}-R_m\frac{\partial g}{\partial V}\right]\right]\times\left[1+\frac{I_{SS}(k_I-R_mk_V)}{\gamma_{SS}(1+\gamma_{SS})}\right]^{-1}\ , \tag{21}$$

ω and κ are the angular frequency and damping constant, and Φ_1 and Φ_2 are phase shifts. Phase shifts have not been extracted from the experimental wave forms and will not be considered further. For the conditions of our experiments and for very small and very large I_{SS}, the roots are real and there are no oscillations, i.e., the system is overdamped. The transitions are discussed in more detail in Sec. III C. As I_{SS} approaches zero, the decay constant approaches $1/(2R_SC)$. One can also determine R_SC experimentally by measuring the voltage transient in the absence of a discharge.

We can define an equivalent lumped-parameter circuit for the discharge. This circuit and the associated circuitry external to the discharge are shown in Fig. 3. Here we define the discharge inductance L by

$$L=\frac{T}{I_{SS}\partial g/\partial V}\left[1+\frac{I_{SS}k_I}{\gamma_{SS}(1+\gamma_{SS})}\right]^2\times\left[1+\frac{I_{SS}k_I}{\gamma_{SS}(1+\gamma_{SS})}\left[1-\frac{k_V}{\gamma_{SS}\partial g/\partial V}\right]\right]^{-1}\ , \tag{22}$$

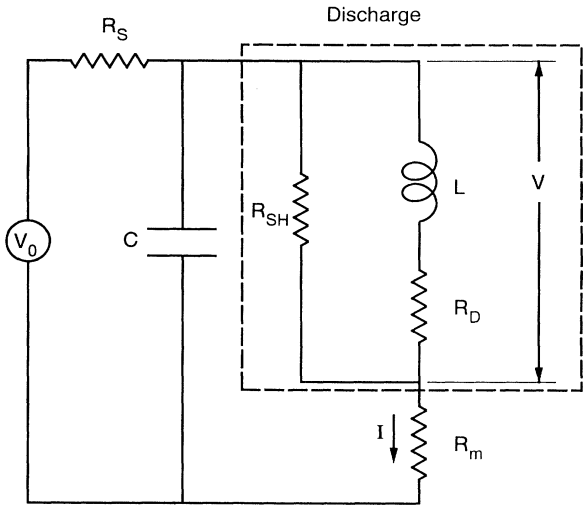

FIG. 3. Equivalent circuit of discharge including the lowest-order effects of a space-charge distortion of the electric field. The dashed rectangle encloses the circuit elements derived from the differential equations used to model the discharge. Note that according to the model both the discharge resistance R_D and the shunt resistance R_{sh} are negative.

the resistance in series with the discharge inductance R_D by

$$R_D=\frac{-k_I}{\gamma_{SS}\partial g/\partial V}\left[1+\frac{I_{SS}k_I}{\gamma_{SS}(1+\gamma_{SS})}\right]\times\left[1+\frac{I_{SS}k_I}{\gamma_{SS}(1+\gamma_{SS})}\left[1-\frac{k_V}{\gamma_{SS}\partial g/\partial V}\right]\right]^{-1}, \tag{23}$$

and a shunt resistance R_{sh} across the discharge by

$$R_{sh}=-\left[\frac{\gamma_{SS}(1+\gamma_{SS})}{I_{SS}k_V}+\frac{k_I}{k_V}\right]. \tag{24}$$

In the limit of small steady-state currents Eqs. (22) and (23) become

$$L=\frac{T}{I_{SS}\partial g/\partial V}, \tag{25}$$

$$R_D=-\frac{k_I}{\gamma_{SS}\partial g/\partial V}, \tag{26}$$

and R_{sh} becomes infinite and can be neglected. The discharge voltage V is that developed across the discharge inductance L and resistance R_D, or equivalently, across R_{sh}.

The equivalent circuit concept has been discussed by many authors [4–16]. In particular, Sigmond [9] has associated the negative resistance labeled R_D in Fig. 3 with the negative slope of the volt-ampere characteristic of the discharge and discharge stability. See Sec. IV A for our derivation of the differential negative resistance. We have not found a published discussion of the negative "internal" shunt resistance R_{sh} given by our model. A positive discharge shunt resistance has been discussed by van Geel [4]. The effect of an "external" shunt resistance on discharge stability and constriction is discussed by Emeleus [14], after an experiment by Güntherschulze and Schnitger [32]. Note that an effect of the negative shunt resistance is to make the impedance vector for the discharge lie entirely in the negative real impedance half plane as the frequency varies in contrast to the usual formulations [4–12] that cross from negative to positive real impedances as the frequency increases. If one includes the external resistances R_S and the total capacitance C in the "discharge" impedance, as appears to be done in most measurements [7,9,10,12,33,34], the impedance versus frequency plot for the "discharge" approximates the conventional form for a resonant circuit. This is because the net resistance shunting the discharge is $R_m+R_SR_{sh}/(R_S+R_{sh})$ and is generally positive.

In the limit of low currents and $\omega^2\gg\kappa^2$, Eqs. (20) and (21) can be written in terms of equivalent circuit elements as

$$\omega^2=\frac{1}{LC}\left[1+\frac{(R_m+R_D)}{R_S}\right] \tag{27}$$

and

$$\kappa=\frac{1}{2R_SC}+\frac{(R_m+R_D)}{2L}. \tag{28}$$

C. Oscillation limits

The current at the boundary for the transition from damped oscillations to underdamped oscillations, i.e., self-sustained oscillations in the dc experiment [1] or growing oscillations in the pulsed experiment [2], is obtained by setting $\kappa=0$ in Eq. (21) to obtain

$$I_{SS}^{tr}=\left[\frac{R_SC}{T}\left[\frac{k_I}{\gamma_{SS}}-R_m\frac{\partial g}{\partial V}\right]+\frac{[(R_S+R_m)k_V-k_I]}{\gamma_{SS}(1+\gamma_{SS})}\right]^{-1}. \tag{29}$$

The dashed line of Fig. 4 shows the application of Eq. (29) to the evaluation of I_{SS}^{tr} versus R_S for $pd=1.05$ Torr cm. As in Fig. 2, we have not plotted current density since the implied scaling fails because the total circuit capacitance C does not vary significantly with the electrode area A in most experiments. Thus, the data of Fig. 4 apply only for $C=250$ pF. The solid circles are data from paper I for the transition from damped to underdamped oscillations. Making use of Eqs. (25) and (26) and noting that for a typically large value of R_SC/T only the first term in Eq. (29) is significant, we obtain

$$I_{SS}^{tr}=\frac{T\gamma_{SS}}{R_SCk_I}\left[1-\frac{R_m\gamma_{SS}}{k_I}\frac{\partial g}{\partial V}\right]^{-1} \tag{30}$$

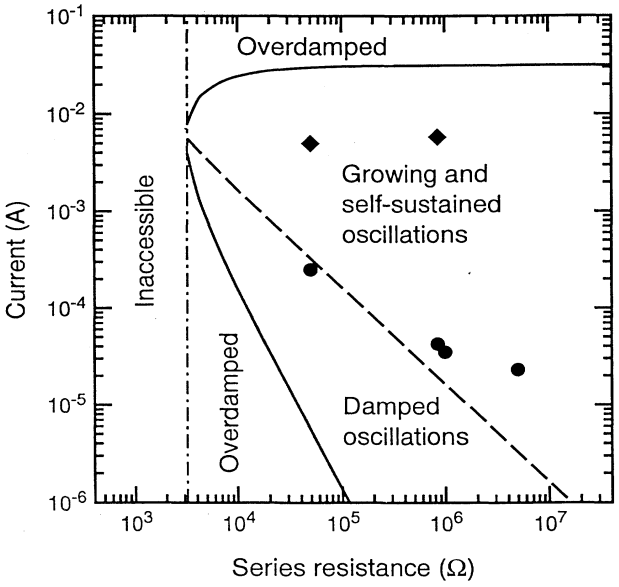

FIG. 4. Stability diagram of current vs series resistance for H_2 discharge. The curves indicate theoretical lower and upper limits for self-sustained or underdamped oscillations and for overdamped oscillations. A region that is inaccessible with our circuitry is also shown. The points are experimental data for the lower limits (●) and upper limits (♦) for oscillations for H_2 discharges with $pd=1.05$ Torr cm from paper I. This diagram is valid only for $C=250$ pF.

or

$$R_S^{\rm tr}=\frac{L}{(-R_D)C}\left[1-\frac{R_m}{(-R_D)}\right]^{-1}. \tag{31}$$

The predictions of Eq. (30) and (31) are almost indistinguishable from those of Eq. (29) for the parameters of Fig. 4. For $R_m=0$, Eq. (32) yields the upper limit of $R_S<R_S^{\rm tr}=L/(-R_DC)$ for a stable discharge given by Sigmond [9]. It should be kept in mind that the small-signal theory developed here to predict these limits yields the discharge parameters for which the oscillation amplitude grows in time and does not describe the large amplitude oscillations.

The two sets of conditions for a transition from damped oscillations to overdamped oscillations are obtained by setting $\omega=0$ in Eq. (20). We will express the results in terms of the values of the steady-state current at the lower current $I_{\rm SS}^{\rm lo}$ and upper current $I_{\rm SS}^{\rm hi}$. In the limit of small dc discharge currents $I_{\rm SS}$, this condition reduces to

$$I_{\rm SS}^{\rm lo}=\frac{T}{4R_SC(R_S+R_m+R_D)}\frac{1}{\partial g/\partial V} \tag{32}$$

or

$$R_S(R_S+R_m+R_D)=\frac{L}{4C}. \tag{33}$$

The theoretically predicted values of $I_{\rm SS}^{\rm lo}$ as a function of R_S for constant R_m are shown by the lower solid curve in Fig. 4 for values of R_D, T, and dg/dV appropriate to the data of paper I for $p=1$ Torr. See the Appendix for further discussion of the discharge parameters used. We have observed this transition in the experiments of II, but have not tested this limit quantitatively against experiment. It may be possible to do so by extrapolating measured frequencies versus current to zero ω [35]. This limit does not appear to have been discussed in the literature, although the region between the limits given by Eqs. (29) and (32) have often been examined by measuring the discharge impedance as a function of frequency [7,9,10,12,33,34].

The high-current solution obtained from Eq. (20) for $\omega=0$ gives a transition from self-sustained oscillations to the decay of current governed by two exponentials. The current calculated for this transition $I_{\rm SS}^{\rm hi}$ is shown by the upper solid curve of Fig. 4, while the experimental values from I are shown by the diamonds. The large discrepancy between theory and experiment shows that the theory is only qualitative at these currents, presumably because of large space-charge effects that violate the assumptions of the first-order model. A further discrepancy between this theory and experiment is observed in paper II. These data show a high-current transition from self-sustained oscillations to damped oscillations, as in the two highest-current data sets in Figs. 4–6 of II, and then to overdamped oscillations at still higher currents. A model of the ac behavior of discharges with well-developed cathode-fall regions, such as found in paper II for H_2 discharges at pressures above 266 Pa (2 Torr), has been given by Ecker and co-workers [13,15]. We have not attempted to apply their model to the experiments of papers I and II.

The left-hand portion of Fig. 4 is marked "inaccessible" because the constant negative differential resistance model says we cannot make measurements in this region with our electrical circuit. Because of the negative resistance behavior represented in the equivalent circuit by R_D and $R_{\rm sh}$ the application of voltages $V_0>V_B$ through a series resistor R_S smaller than $R_DR_{\rm sh}/(R_D+R_{\rm sh})$ results in an increase of discharge current to values such that our models are no longer valid. This behavior is thoroughly discussed in the literature [3–16]. Note that the constant negative resistance assumption fails at the higher discharge currents and limits the inaccessible region as illustrated in Figs. 3 and 4 of paper I and Fig. 3 of paper II.

According to Eq. (21) or Eq. (28) when $R_m>R_D$ the damping constant κ is positive for all currents so that spontaneous or undamped oscillations do not occur. This means that by the use of a sufficiently large value of R_m in the experimental apparatus of papers I and II, we should be able to measure the oscillation-free, voltage-current characteristic for the complete range of currents. For example, such experiments would determine the range of currents for which R_D is a negative constant. Recent pulsed experiments [29] verify the predicted suppression of undamped and growing oscillations over a much wider range of discharge currents than shown in Fig. 4 and in Fig. 3 of papers I and II.

D. Current growth coefficient

It is convenient to express the discharge parameter describing the rate of change of gain with voltage $\partial g/\partial V$ and the effective ion transit time in terms of a "current growth" coefficient defined by

$$\frac{\hat{g}}{nT} \equiv \frac{1}{nT}\frac{V}{g}\frac{\partial g}{\partial V} . \tag{34}$$

This coefficient is normalized to the gas density to make it dependent only on E/n and nd (or V and nd) for a given gas and electrode combination. Note that since this parameter is evaluated for a steady-state, self-sustained discharge, $g=1$ in the denominator of Eq. (34). The discharge parameter describing the effects of space charge, i.e., the negative differential resistance, will be discussed in Sec. IV.

A source of growth coefficient data is the measured growth of current following the application of a voltage pulse to the circuit of Fig. 1. Because of the relatively large external capacitance C across the discharge, the voltage across the discharge begins to approach the steady-state exponentially with time with a time constant $R_S C$. Initially the voltage increases linearly with time. In the absence of photoelectrons, for low currents, and for $t >> T$, Eq. (10) becomes

$$\frac{dI}{dt} = \frac{(g-1)I}{T} = \frac{1}{T}\frac{\partial g}{\partial V}\Delta V(t) I . \tag{35}$$

The solution of Eq. (35) for $\Delta V(t) = at$ is given in Eq. (6) of II and is fitted to measurements for initial currents I_0 of 5 and 100 μA and final currents up to 10 mA in Fig. 10 of II. The fit yields a value of $\hat{g}/nT$ of 5.1×10^{-16} $V^{-1}s^{-1}$ for $pd=1.05$ Torr cm and $V=350$ V. This result is shown by the cross-in-diamond symbol in Fig. 5.

A second source of current growth data is from values of ω or $(LI_{SS})^{-1}$. According to Eqs. (25) and (27) $\hat{g}/nT$ can be obtained from LI_{SS} determinations, such as shown in Fig. 8 of II, or from the angular frequency measurements shown in Fig. 9 of I and Fig. 5 of II. The results of such determinations from paper II are shown as a function of E/n in Fig. 5. In this figure the solid line connects data points from paper II.

Current growth coefficient data for H_2 are also available from published measurements of the formative time lag [36] and from the e-folding time τ characteristic of the exponential growth of current predicted by Eq. (35) when a step function of voltage is applied to the discharge [36,37]. Thus, in Eq. (35) we define $\tau = T/(g-1)$ and find

$$\frac{\hat{g}}{nT} = \frac{1}{n\tau}\frac{V}{\Delta V} . \tag{36}$$

The experiments of Graf and Schmitz [37] yield values of $\tau\Delta V/V$ that are approximately constant for a given E/n and pd. These data are used to calculate the open circles of Fig. 5.

The dashed and dot-dashed lines in Fig. 5 show approximate lower and upper limits, respectively, to the growth constant for $E/n < 300$ Td. The lower limit is calculated using the ionization coefficient and ion-induced electron yield data discussed in the Appendix to calculate g and $\partial g/\partial V$ and using ion drift velocity data for H_3^+ [38] to calculate T for E/n below that for H_3^+ runaway and breakup [38]. The dot-dashed curve is an estimate of the growth coefficient for photon-induced electron emission as calculated using a typical radiative lifetime of 10 ns for T in Eq. (34). The value of $\hat{g}=1$ was used so that the dot-dashed curve is an upper limit to the growth constant. The use of more realistic values of $\hat{g}$ taking into account the distributed source of uv radiation would significantly lower this upper limit. Several authors [36,37] have used formative time lag and current growth time constant data for hydrogen to estimate the contributions of photon-induced electron emission and of ion-induced electron emission to γ.

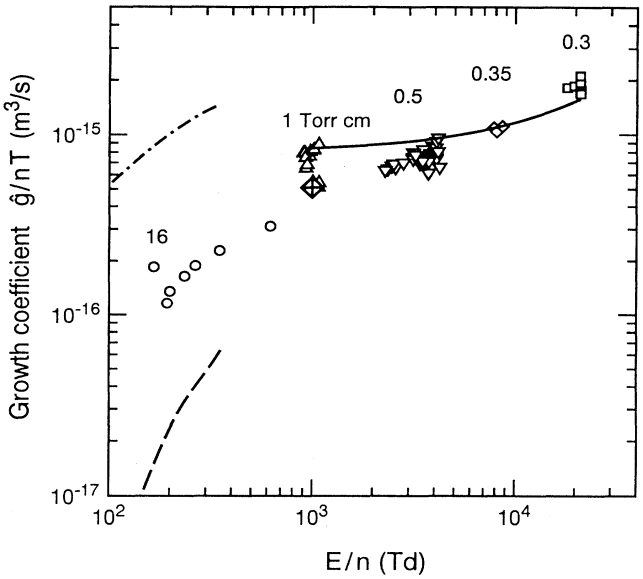

FIG. 5. Current growth coefficient $\hat{g}/nT$ vs E/n. The points are from data such as shown in Fig. 8 of II: □, 0.3 Torr; ◇, 0.35 Torr; ▽, 0.5 Torr; △, 1 Torr, and from current growth measurements: ○, Ref. [37]. The cross-in-diamond point is from the fit shown in Fig. 10 of II. The solid line connects the lower-pressure data of paper II. The results of the analytical equilibrium model are shown by the dashed and dot-dashed lines. The numbers give the pd values associated with the nearby data points.

At the higher E/n of Fig. 5 a smooth solid curve is drawn through the growth constant data chosen in papers I and II to represent the oscillation results. We do not show a theoretical curve for $\hat{g}/nT$ at high E/n because we have no independent measurement of the values of the effective ion transit time T. The high value of $\hat{g}/nT$ for $p=1$ Torr is the result of our choice of data for low currents and aged cathodes.

E. Variation with cathode condition

Figure 6 shows the variation of the current growth coefficient with the breakdown voltage V_B and its equal,

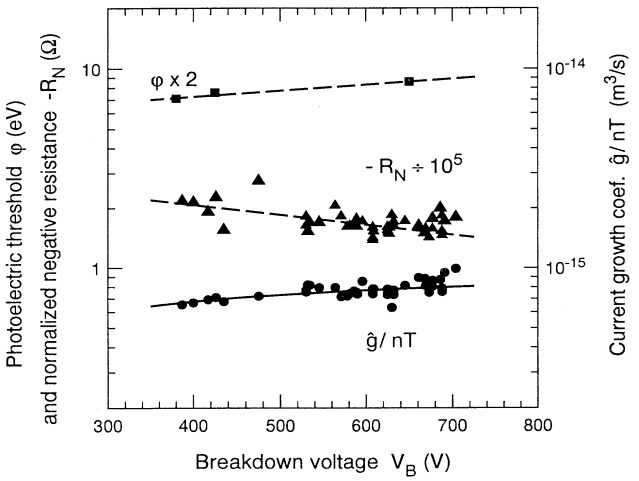

FIG. 6. Plot of current growth coefficient $\hat{g}/nT$, photoelectric threshold energy φ, normalized discharge negative resistance $-R_N$ vs breakdown voltage showing the effects of changes in the cathode condition. The points are experimental results from II for $p=0.5$ Torr. The solid curve is calculated from the model of Sec. III D. The dashed lines are arbitrary curves through the data.

the low-current limit of the maintenance voltage, as the cathode is aged at 0.525 Torr cm. Here the breakdown voltage is our day-to-day experimental measure of the cathode condition [1,2]. The solid circles are $\hat{g}/nT$ values calculated from the LI_{SS} data from paper II. The solid line shows the results of the application of the equilibrium model to the evaluation of $\hat{g}/nT$ versus V. See the Appendix for details. At the high E/n ($\approx$4000 Td) of these experiments, $\hat{g}/nT$ increases with voltage because the ion transit time T decreases more rapidly with increasing voltage than the normalized change in loop gain $\hat{g}$ decreases with increasing voltage.

Also shown in Fig. 6 are the values of the photoelectric threshold (solid squares) as measured in paper II. We see that the increase in photoelectric threshold and the increase in breakdown voltage are consistent with a reduced escape probability of electrons from the cathode surface as the work function increases [36,39].

It should be kept in mind that the very large range of steady-state, low-current discharge voltages shown in Fig. 6 is unusual. This condition results from the slow variation of the effective α/n and, therefore, g with E/n and the resulting high sensitivity of the discharge voltage V to changes in γ with cathode aging.

IV. DIFFERENTIAL RESISTANCE AND CAPACITANCE

In this section we will calculate the negative differential resistance of the discharge R_D and the differential capacitance C_D caused by space-charge distortion of the electric field. The exact calculation of the effects of space charge on the electric field in a moderate and high current electric discharge is very difficult. Several treatments [8,15,21,40] of discharges in parallel-plane geometry have dealt with the limit of a well-developed cathode fall. These models either use an assumed electric-field variation with position or calculate the self-consistent electric field. Here we calculate the self-consistent electric field, but limit the discharge current so that the perturbation of the applied electric field is small. We first present an analytic model applicable when the behaviors of the electrons and of a single type of ion are determined by the local electric field, as in the case of discharges at moderate E/n in Ar [25,41,42] or in H_2 at $E/n \leq 300$ Td [43]. We then present the results of a numerical model applicable to hydrogen at high E/n, when the electrons and ion motion may not be in equilibrium with the local electric field and when several ions may be present. A summary of our model for H_2 discharges involving nonequilibrium motion of electrons, hydrogen ions, and hydrogen neutrals appears in Ref. [44].

A. Local-equilibrium model of differential resistance

Experiments have shown that in H_2 discharges at low currents for both low pressures [2,9,16,19] and high pressures [18] the discharge voltage decreases linearly with increasing current for small voltage changes. This behavior corresponds to a constant negative differential resistance. We have not found any quantitative predictions of this effect or any comparisons with experiment, although there are several models of the closely related measurements of the lowering of the breakdown potential by large photocurrents emitted from the cathode [16–19].

We will therefore limit our model to a first-order perturbation from the low-current limit of discharge operating voltage or breakdown voltage. This means that we can calculate the space charge to first order using the steady-state ion and electron current densities from Sec. III appropriate to a spatially uniform electric field. This is done through Poisson's equation and the assumption that the electron density is small compared to the positive ion density. The space-charge-induced electric field E_S is found by solving the one-dimensional space-charge equation

$$\frac{dE_S}{dz}=\frac{e}{\epsilon_0}(n_p-n_e)\approx\frac{J}{\epsilon_0 W_+}[1-e^{\alpha_0(z-d)}]\ , \tag{37}$$

and the relation between electric field and voltage change δV_S, i.e.,

$$\frac{d\delta V_S}{dz}=-E_S(z)\ . \tag{38}$$

Here n_+ and n_e are the positive ion and electron densities, ϵ_0 is the permittivity of free space, J is the total current density, W_+ is the positive ion drift velocity, α_0 is the value appropriate to the unperturbed electric field, and the positive electric field is directed from anode to cathode. The resultant difference in electric field is

$$E_S-E_C=\frac{J}{\epsilon_0 W_+\alpha_0}[\alpha_0 z-e^{\alpha_0(z-d)}+e^{-\alpha_0 d}]\ , \tag{39}$$

where E_C is the electric field at the cathode. This same

result is obtained using the more general calculation of the electric field of Crowe, Bragg, and Thomas [17] and then expanding their result in terms of small changes in the electric field from E_C. The corresponding change in voltage between the cathode and anode δV_S is then

$$\delta V_S = -\int_0^d (E_S - E_C)dz = -\frac{Jd^2}{\epsilon_0 W_+}\left[\frac{1}{2}+\frac{e^{-\alpha_0 d}}{\alpha_0 d}-\frac{(1-e^{-\alpha_0 d})}{(\alpha_0 d)^2}\right] . \quad (40)$$

The difference in electric field $E_S - E_C$ and potential change δV_S caused by the space charge must next be related to the changes in electric field at an electrode. Note that in Eq. (40) W_+ and α/n are dependent on E/n.

The second part of the derivation is the evaluation of the change in the electric field at the cathode E_C from the unperturbed field E_0. This is accomplished using the condition that the electric field at the cathode must be such that the round-trip electron number gain is unity, i.e., that g in Eq. (4) equals 1. Since this calculation is for moderate E/n, we assume $\delta=0$, although its effect could be considered [25]. We first expand α and γ in terms of small changes in the electric field from the unperturbed field, i.e.,

$$\alpha(z)=\alpha_0-\frac{d\alpha}{d|E|}[E_S(z)-E_0] \quad (41)$$

and

$$\gamma=\gamma_0-\frac{d\gamma}{d|E|}[E_C-E_0] , \quad (42)$$

where the signs are chosen to make α and γ increase when $d\alpha/d|E|$ and $d\gamma/d|E|$ are positive and the magnitudes of the negative electric fields increase. Here $d\gamma/d|E|$ is appropriate for ion-induced electron emission from the cathode when the ion energy is determined by the E/n at the cathode. Note that in Eq. (42) $\gamma_0=\gamma_p+k_V V_B$, as calculated from Eq. (8) for $V=V_B=|E_0|d$ and $I=0$, i.e., for the unperturbed electric field. Substitution of Eqs. (41) and (42) into the maintenance condition gives

$$1=\gamma[\exp(\int\alpha\,dz)-1] = \left[\gamma_0-\frac{d\gamma}{d|E|}(E_C-E_0)+\cdots\right] \times\left[e^{\alpha_0 d}-1-e^{\alpha_0 d}\frac{d\alpha}{d|E|}\int_0^d(E_S-E_0)dz+\cdots\right] . \quad (43)$$

Utilizing the unperturbed discharge maintenance condition that $1/\gamma_0=\exp(\alpha_0 d)-1$ and keeping only terms to first order in E_C-E_0, we obtain

$$\delta V \equiv -\int(E_S-E_0)dz=\delta V_S-(E_C-E_0)d = \frac{\hat{\gamma}}{\hat{\gamma}+\gamma\alpha d e^{\alpha d}\hat{\alpha}}\delta V_S , \quad (44)$$

where

$$\hat{\gamma}=\frac{(E_C/n)}{\gamma}\frac{d\gamma}{d(E_C/n)} \quad (45)$$

and

$$\hat{\alpha}=\frac{(E/n)}{(\alpha/n)}\frac{d(\alpha/n)}{d(E/n)} . \quad (46)$$

Note that $\hat{\gamma}$ and $\hat{\alpha}$ are the slopes of log-log plots of γ and α/n versus E/n and are evaluated at E_0/n. For scaling purposes it is convenient to define a normalized negative differential resistance given R_N in terms of the differential resistance R_D of Sec. III by

$$R_N \equiv \frac{A\delta V}{Id^2}=\frac{AR_D}{d^2}=-\frac{\hat{\gamma}f(\alpha d)}{\epsilon_0 W_+\hat{g}} , \quad (47)$$

where A is the electrode area and $f(\alpha d)$ is equal to the square bracket in Eq. (40). We have dropped the subscript 0 on α and used the fact that from Eq. (4) one can write $\hat{g}=\hat{\gamma}+\gamma\alpha d\exp(\alpha d)\hat{\alpha}$. Equation (47) shows that the normalized negative differential resistance R_N caused by changes in the electron yield at the cathode goes to zero as $\hat{\gamma}$ goes to zero and so is consistent with previous proofs of no linear change in V with current caused by space-charge-induced changes in α [6,8,16,17,27]. This equation also shows that for a given set of electrode and gas parameters, R_N is a function of the variables $W_+(E/n)$, $\alpha/n(E/n)$, and γ and so is a function of the usual low-current discharge variables, i.e., pd (or nd) and V or one of these and E/n. Equations (47) and (26) can be used to evaluate k_I as

$$k_I=\frac{d^2 f(\alpha d)\gamma\hat{\gamma}}{AV_0\epsilon_0 W_+}=\frac{df(\alpha d)}{A\epsilon_0 W_+}\frac{d\gamma}{d|E|} , \quad (48)$$

where $d\gamma/dE$ is evaluated at E_0/n.

We obtain the same results if γ is assumed to depend on V_C rather than on E/n at the cathode provided that $\hat{\gamma}=(V_B/\gamma_0)d\gamma/dV$. This assumption would be appropriate for ions undergoing free-fall motion across the gap, as expected at the higher E/n. Note that it would be essential to include the change in δ with V for very high E/n [25]. We have not derived the negative differential resistance for the case of photon-induced electron emission appropriate to the lower E/n, where the change in photon flux reaching the cathode is dependent on changes in field throughout the gap [6,8,16–18,27,36].

Note that R_D is proportional to the proper variable Jd^2 or the combination $(J/n^2)(nd)^2$, where J is the discharge current density. This variable, along with the V and nd (or E/n and nd) variables used for very low-current discharges, completes the set obtained from most models of moderate-current discharges that do not include processes such as electron-ion recombination or ionization of excited states [6,8].

The predictions of our model of the normalized negative differential resistance are compared with published experimental data [9,18,19] and data from papers I and II in Fig. 7 for low-current hydrogen discharges. The pd values vary from 800 to 0.3 Torr cm as the E/n increases from 64 Td to 4.2 kTd. The choice of ion transit times used to calculate the effective W_+ is critical at very high

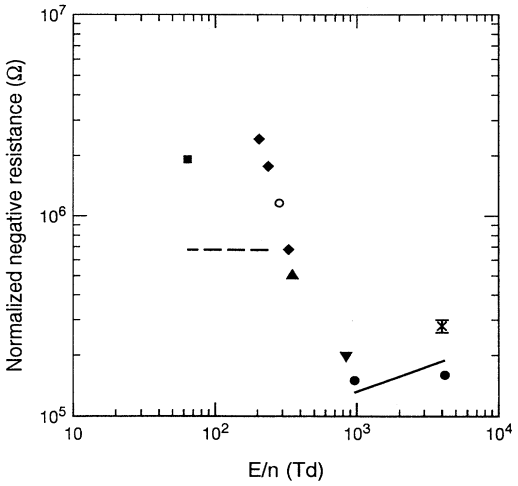

FIG. 7. Normalized negative differential resistance vs E/n. The solid points are from experiment: ▲, paper I; ●, paper II; ♦, Ref. [9]; ■, Ref. [18]; ▼, Ref. [19]. The result of our numerical calculation is shown by the × and that of Ref. [18] by the ○. The dashed line shows results of the analytic model using ion transit times T calculated from the H_3^+ drift velocity, while the solid line shows model results using T values from fits to damped oscillation measurements.

E/n, where the equilibrium model begins to fail because of runaway ion motion [28]. We see from the solid curve of Fig. 7 that the use of transit times obtained from fits of the model of Sec. III and the coefficients of the Appendix results in good agreement of the theory and experiment for R_N at $E/n > 700$ Td. R_N varies rapidly for E/n between 200 and 300 Td. This is the region of rapidly increasing γ with increasing E/n because of the transition from photon-induced to the more efficient ion-induced electron emission at the cathode [18,19,36]. At low E/n we have calculated R_N using the relation $W_+ = 30E/n$, based on the data for H_3^+ in Ref. [28], and have assumed $\hat{\gamma}=1$ in order to get some estimate as to R_N values. A slow variation of R_N with E/n is calculated for both low E/n and high E/n, because of the small changes in effective ion transit times within these limiting E/n regions. The surprising thing to us is that the experimental R_N values at $E/n < 200$ Td are larger than calculated, even with the seemingly extreme assumption of $\gamma=1$. Experiment suggests γ is approximately constant so that $\hat{\gamma}$ is small [29,36,37].

The negative differential resistance calculated for H_2 discharges at intermediate E/n by Ward and Jones [18] is shown by the open circle in Fig. 7. These calculations assume equilibrium ionization and includes the rapid variation of γ with E/n extracted from breakdown data. The calculated value agrees with their experiment to within the experimental uncertainties. An effective differential resistance can also be estimated from the calculations of the effects of space charge on the breakdown of H_2 at low E/n by DeBitetto, Fisher, and Ward [18]. Since these authors assume $\hat{\gamma}=0$, their mechanism appears to be very different from ours. This point needs further investigation.

B. Nonequilibrium calculations

These calculations are carried out with the numerical model of low-current nonequilibrium hydrogen discharges used to analyze Doppler broadened emission from H_2 discharges at very high E/n [44]. The calculations are rather tedious since it is necessary to iterate on the assumed value of the electron energy and the assumed value of the electric field at the anode so as to obtain a reasonable initial energy for the electrons leaving the cathode (0.5 eV), while at the same time satisfying the maintenance condition that $1/\gamma$ at the E/n at the cathode must equal the ion production per electron leaving the cathode.

The electric field and normalized electron flux distributions resulting from the space charge for an H_2 discharge operating at a current density of 2 A/m^2 or a current of 10 mA for our 50 cm^2 are shown by the solid curves in Fig. 8. Here J_e is the electron current density normalized to the total current density. The calculated decrease in voltage necessary to keep $g=1$ is 48 V for an initial discharge voltage of 600 V. These results are to be compared with the results of calculations shown by the dashed curves for a discharge current density that is small enough so that space-charge effects can be neglected, i.e., for 2×10^{-3} A/m^2 or 10^{-5} A for our discharge. Note that the small increase in $J_e(0)$ at the cathode is equal to the increase in $\gamma/(1+\gamma)$ caused by the increased magnitude of the electric field at the cathode, while the

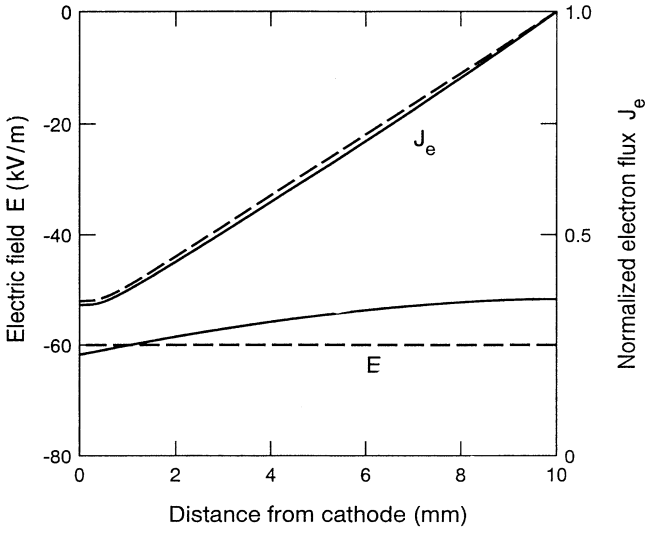

FIG. 8. Electric fields and normalized electron currents caused by positive ion and electron space charge. The solid curves are for a current density of 200 μA/cm^2 discharge in H_2 for a pressure of 67 Pa (0.5 Torr) and a breakdown voltage of 600 V. This corresponds to $I_{SS}=10$ mA for our 50 cm^2. The dashed lines are the essentially unperturbed electric field and electron current for a current density of 2×10^{-7} A/cm^2. The loop gain g is equal to 1 in both cases.

decrease in $1/J_e(0)$ gives the decrease in electron multiplication per avalanche. Also note that at the high E/n of this calculation, nonequilibrium electron behavior causes the increase in electron current with distance from the cathode to be more nearly linear [25] than in the conventional exponential growth for electrons in equilibrium with the field [6]. As shown in Fig. 4 of II the calculated voltage changes versus current are from 1.5 to 2 times the experimental values. Considering the number of assumptions of the model, this is rather good agreement. If we force the ion-induced electron yield to remain constant as the current and space charge are increased, the voltage changes are much smaller, e.g., about 20% of the values cited, and correspond to a negative resistance of about 1000 Ω.

One concern regarding the application of the steady-state model derived in this section to the oscillation problems discussed earlier is that we have assumed that the time delay characteristic of space-charge buildup is short compared to the times characteristic of changes in current and voltage. An assessment of the error resulting from this approximation will have to await more detailed models.

The measured values of R_D reported in II are subject to wide variations as the discharge tube is processed, presumably caused by changes in the cathode condition. The sensitivity to the cathode condition follows from Eq. (26) where R_D is directly proportional to the rate of change in the electron yield with current, i.e., with the change in electric field at the cathode caused by space-charge distortion. The value of R_D may be more sensitive to surface conditions than is $(1/T)(\partial g/\partial V)$ because the partial cancellation of changes in γ through opposite changes in the effective value of $\exp(\alpha d)$ in Eq. (4). See Refs. [17] and [25].

C. Equilibrium model of differential capacitance

In this section we calculate the change in discharge capacitance with discharge current density, i.e., the differential capacitance resulting from the first-order space distortion obtained using the equilibrium ionization model of Sec. III and Sec. IV A. Although several authors have published calculations of the change in discharge capacitance for well-developed cathode falls [13,15], we have not found such calculations for low discharge current densities.

The first-order change in discharge capacitance is obtained from the change in charge on the cathode using the relation

$$\frac{\delta C}{C_D}=\frac{\delta Q}{V_0 C_D}=-\frac{A\epsilon_0(E_C-E_0)}{V_0 C_D}$$
$$=\frac{jd^2}{\epsilon_0 W_+ V_0}\frac{\alpha d\gamma e^{\alpha d}\hat{\alpha}}{\hat{g}}f(\alpha d)\,, \tag{49}$$

where $C_D=A\epsilon_0/d$ is the capacitance of the discharge electrodes and $V_0=V_B=-E_0 d$. Note that the fractional change in discharge voltage calculated from the negative differential resistance R_N relative to $\delta C/C_D$ increases as $[\alpha d\gamma\exp(\alpha d)\hat{\alpha}]/\hat{\gamma}$, i.e., $\delta C/C_D$ increases when the space-charge field causes a large change in the collisional ionization. The contribution of the differential capacitance to the oscillatory behavior of the discharges discussed in papers I and II is limited by the shunted effect of the large capacitance of the leads to the discharge [30] and is neglected throughout this paper.

V. DISCUSSION

We have developed models of the cathode regions of low-current, low-pressure (≈0.3 to 3 Torr) discharges in hydrogen that are useful over a wide range of discharge operating modes and parameters. The steady-state model includes electron- and ion-induced ionization, ion-induced electron production at the cathode, ion-molecule reactions, and space-charge distortion of the electric field. These and the simplified time-dependent differential equations are solved with a nonlinear equation program.

The transient model has only three adjustable parameters determined from experiment for each pressure. The ion-induced electron emission yield (1) and the discharge negative differential resistance (2) are evaluated by fitting the model to dc voltage-current data at low currents so as to allow for changes in the cathode surface with aging. The common time scale (3) is set by the positive-ion transit time and can be obtained by fitting the oscillation model to one of the damped oscillation wave forms or to an average of the oscillation frequencies. All other common parameters, e.g., ionization coefficients, are obtained from published data. Since the magnitude of the applied voltage pulse was not measured for each wave form in II, it is set to fit the model to the experimental current at some convenient instant of time, e.g., the quasi-steady-state current at the end of the pulse. The magnitude of the photoelectron current pulse in the transient data of I is adjusted to fit the initial peak of the oscillating current.

The time-dependent model gives quantitative agreement with experiment with no additional fitting for five discharge modes: the transition from stable discharge operation to spontaneous oscillations shown in Figs. 3–5 of I and Fig. 3 of II; oscillations following a laser-induced photoelectron pulse from cathode as in Fig. 8 of I; oscillations produced by a voltage pulse applied to discharge shown in Fig. 2 of II and Fig. 2 of III; current growth immediately following the application of voltage to gap as in Fig. 10 of II; and spontaneous oscillation voltage and current wave forms shown in Fig. 6 of I. The equilibrium and nonequilibrium steady-state models give approximate agreement with experimental negative differential resistance data over a wide range of discharge pressures, as in Fig. 4 of II and Fig. 7 of III.

The low-frequency damped and self-sustained oscillations observed and analyzed in this series of papers are characteristic of ion transit times. These oscillations occur because of the large resistance and the capacitance of the external circuit. With only the inherent electrode capacitance the frequency of the oscillations would be so high that our model may not apply. For unknown reasons, the wave forms obtained in papers I and II did not show the high-frequency oscillations found by Mitchell *et al.* [20]. Possibly the high frequencies of

these oscillations are determined by the photon-feedback process and could be analyzed by a model similar to that used here for ion feedback.

The effect of the space-charge field on the dc discharge voltage for small currents can be described as that of a negative differential resistance. At high E/n the magnitude of this negative resistance and its variation with E/n are consistent with a model in which the ion-induced electron yield γ varies with the electric field at the cathode, as suggested by Rogowski [16]. Our very approximate extension of the model to low E/n where photon-induced electron emission is dominant suggests that this approach should be examined further.

It should be kept in mind when more than one ion form is present, e.g., H^+, H_2^+, and H_3^+ in hydrogen discharges, the effective ion transit time d/W_+ appearing in the space-charge equations of Sec. IV is to be weighted by the density of the ion species present. On the other hand, in the model of charged particle transients of Sec. III, the effective d/W_+ is weighted by product of the ion-induced electron emission yields and the ion fluxes. This means that H_2^+ and H_3^+ tend to dominate in the space-charge model, while H^+ (and H) tend to dominate in the oscillation model. Also, when the model of Sec. III is extended to approximate photon-induced electron emission conditions by replacing d/W_+ by the excited-state lifetime, the transit time d/W_+ of the space-charge relations of Sec. IV remains that of the ions.

Our recent work [29,45] is concerned with discharge current densities up to about 1 mA/cm^2, where space-charge distortion of the electric field is large. As the current increases above the range of the present paper, the differential discharge resistance departs from a negative constant and eventually becomes positive.

Note added in proof. It has recently come to our attention that Melekhin and Naumov have previously presented a perturbation analysis of the low-current diffuse discharge. These authors derive the negative differential voltage versus current characteristic through second order in current and find the discharge current for the onset of self-sustained oscillations. They obtain consistency with a set of experimental data for neon. Their analytical results for low currents agree with ours for the small γ and large $\exp(\alpha d)$ appropriate to our higher-pressure discharges, but are not applicable for the large γ and $\exp(\alpha d)$ near unity characteristic of our lower-pressure discharges. Our extension of the theory to describe transient experiments leads to tests of the model over a much wider range of discharge parameters and allows the determination of additional discharge characteristics such as the effective ion transit time. See V. N. Melekhin and N. Yu. Naumov, Zh. Tekh. Fiz. **54**, 1521 (1984) [Sov. Phys. Tech. Phys. **29**, 888 (1984)].

ACKNOWLEDGMENTS

The authors thank A. Gallagher, A. Garscadden, J. H. Ingold, and R. J. Seeböck for helpful discussions. This work was supported in part by the National Institute of Standards and Technology, the U.S. Air Force Wright Laboratories, and the U.S.-Yugoslavia Joint Board, Project 926.

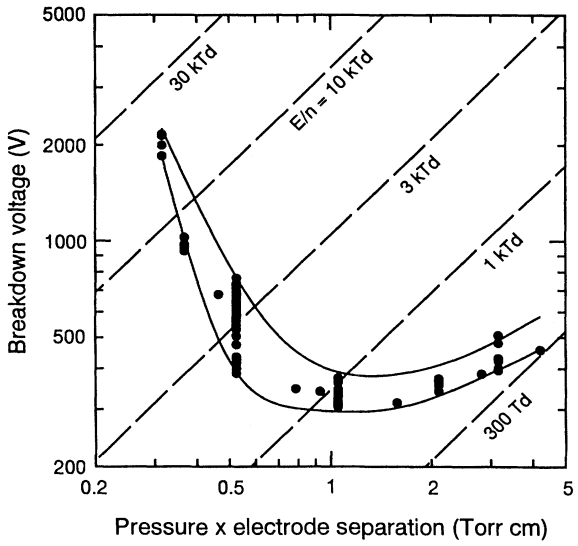

FIG. 9. Low-current maintenance and breakdown voltages V_B vs pressure-electrode separation product pd for H_2 and the $d=1.05$ cm parallel-plate discharge tube used in the experiments analyzed in this paper. The smooth curves are the approximate limits of the observed voltages shown by the points. The higher voltages generally result from longer aging of the cathode.

APPENDIX: DISCHARGE PARAMETERS

The low-current maintenance voltage or breakdown voltage used in the experiments of papers I and II are shown in Fig. 9 as a function of the pressure-electrode separation product pd. They are shown to illustrate the wide range of discharge operating conditions encountered and to emphasize the need for a technique to determine the parameters, such as the effective electron yield per ion, applicable for each set of voltage and current transients analyzed. Note especially the 2:1 range of operating voltage for $pd=0.5$ Torr cm for our gold-plated copper cathode and a graphite anode. The procedure for determination of the parameters discussed in this appendix is to use published ionization coefficient data to determine γ from the measured breakdown voltages V_B. The yields are then approximated by an algebraic formula and used in the differential equations and analytic relations of Secs. III and IV for comparison with experiment.

The spatial ionization coefficient for electrons used is

$$\frac{\alpha}{n}=\frac{1.4\times10^{-20}\exp[-405/(E/n)]}{[(10^{-4}E/n)^{1.5}+1]^{0.5}}\ , \tag{A1}$$

where α/n is in m^2 and E/n is in Td. This coefficient is strictly valid only for low enough E/n, e.g., ≤ 1000 Td for H_2, so that the electrons are in equilibrium with the local electric field [6,25]. We use this relation at the higher E/n shown in Fig. 9 since experiment [43] shows that the deviations from exponential growth are accept-

TABLE I. Parameters used in models of low-current parallel-plane H_2 discharges with $C=250$ pF, $A=50$ cm^2, $d=1.05$ cm.

p (Torr)	0.3	0.35	0.5	0.5	1.0	3.0
V_B (V)	2050	1025	390	700	350	410
Expt. R_D (Ω)	-830[a]	-2500[a]	-1500[b]	-3700[b]	-4500[a]	$-10\,000$[c]
E/n (kTd)	20.5	9.1	2.4	4.4	0.97	0.41
$\partial\gamma/\partial V$ (V^{-1})	3.5×10^{-4}	4.2×10^{-4}	4.8×10^{-4}	2.6×10^{-4}	1.3×10^{-4}	1.3×10^{-5}
$\partial\gamma/\partial I$ (A^{-1})	0.16	0.86	0.83	0.86	1.23	0.81
γ	0.71	0.43	0.19	0.18	0.056	0.0054
$\hat{\gamma}$	1	1	1	1	1	1
$\partial g/\partial V$ (V^{-1})	0.000 32	0.000 64	0.0031	0.0014	0.0072	0.015
α/n (m^2)	6.9×10^{-21}	9.8×10^{-21}	1.12×10^{-20}	1.13×10^{-20}	9.5×10^{-21}	5.2×10^{-21}
$T/(\partial g/\partial V)$ (s V)[d]	1.2×10^{-4}	7.6×10^{-5}	3.5×10^{-5}	5.3×10^{-5}	1.45×10^{-5}	e
T (μs)	0.02	0.06	0.11	0.07	0.08	e

[a]Average values for all V_B.
[b]From smooth curves through data of Fig. 8 of paper II.
[c]Reference [29].
[d]Averages from experiment.
[e]Insufficient data available.

able at our E/n and pd and since we have not yet developed analytical expressions appropriate to this nonequilibrium situation [25]. Limited calculations using the numerical nonequilibrium model for H_2 yield values for the ions reaching the cathode per electron leaving, i.e., the effective value of g, that are 1.5 times those calculated using Eq. (A1) for $p=0.5$ Torr and the highest measured discharge voltage of 700 V.

Note that the particularly wide range of breakdown voltages observed for $pd\approx0.5$ Torr cm corresponds to $E/n\approx3$ kTd and the maximum of the α/n versus E/n values given by Eq. (A1). From Eq. (4) we see that small changes in the magnitude of γ caused by changes in the cathode condition, shown by the photoelectric threshold in Fig. 6, will require relatively large changes in V and E/n.

The ion-induced electron yield at the cathode is approximated by rewriting Eq. (8) as

$$\gamma=0.001+\frac{\partial\gamma}{\partial V}V+\frac{\partial\gamma}{\partial I}I\ , \tag{A2}$$

where $k_V=\partial\gamma/\partial V$ and $k_I=\partial\gamma/\partial I$ from Sec. III and γ_p has been given inconsequential value of 0.001. The values of $\partial\gamma/\partial V$ are adjusted to give the observed breakdown voltage V_B when using Eq. (A1) for the ionization. The values of $\partial\gamma/\partial I$ are adjusted to give the observed negative differential resistances using Eq. (26). The results of these adjustments are given in Table I.

The effective ion transit time at a given pressure is assumed to vary as V^m, where $m=0.8$. Such a variation is intermediate between the $m=0.5$ expected for free fall of the ions and $m=1$ expected for constant ion mobility [6] and fixed pressure.

Our choice of the ion yield per electron arriving at the anode δ is so small, i.e., $\delta=0.1$, that it is almost negligible. The experimental yields of backscattered electrons [46], i.e., electrons with energies greater than 25 eV, for graphite are quite variable, but are typically 0.2 for 500 eV incident electrons, so that the yield of ions will be smaller. For heavy metal targets the yields are generally higher than for graphite. For E/n higher than considered here δ will become increasingly important [25].

In summary, the procedure used in fitting the model to the damped oscillation data is to use γ results with Eqs. (25) and (27) to estimate T. After several iterations using the more exact formulas, one arrives at a consistent set of values of k_V, k_I, T, and $\partial g/\partial V$ for use in generating the small-signal model results for a particular pressure. For the numerical calculations of Sec. III A, formulas for $\alpha/n(E/n)$, $\gamma(V)$, and $T(V)$ and average values of R_D and V_B for a given pressure and cathode history are used along with a run-specific value of the quasi-steady-state current or the peak value of the photoelectric current pulse.

*Also with Physics Department, University of Colorado, Boulder, CO 80309-0390.
†Present address: Institute of Physics, P.O. Box 68, Zemun, Yugoslavia.

[1] Z. Lj. Petrović, and A. V. Phelps, this issue, Phys. Rev. E **47**, 2806 (1993); referred to as paper I.
[2] B. M. Jelenković, K. Rózsa, and A. V. Phelps, preceding paper, Phys. Rev. E **47**, 2816 (1993); referred to as paper II.
[3] W. Kaufmann, Ann. Phys. (Leipzig) **2**, 158 (1900).
[4] Chr. van Geel, Physica **6**, 806 (1939); Chr. van Geel, Appl. Sci. Res. **85**, 79 (1956).
[5] H. Gawehn, Ann. Phys. (Leipzig) **20**, 601 (1934).
[6] M. J. Druyvesteyn and F. M. Penning, Rev. Mod. Phys. **12**, 87 (1940).
[7] C. J. D. M. Verhagen, Physica **8**, 361 (1941).
[8] G. Francis, Handb. Phys. **22**, 53 (1956).
[9] R. S. Sigmond, in *Proceedings of the Fourth International Conference on Ionization Phenomena in Gases, Uppsala, 1959,* edited by N. R. Nilsson (North-Holland, Amsterdam, 1960), p. 189; in *Proceedings of the Fifth-International Conference on Ionization Phenomena in Gases, Munich, 1961,* edited by H. Maecker (North-Holland, Amsterdam, 1962), p. 1359; in *Proceedings of the*

Ninth International Conference on Ionization Phenomena in Gases, Bucharest, 1969, edited by G. Musa, I. Ghica, A. Popescu, and L. Nästase (Institute of Physics, Academy of the Socialist Republic of Roumania, Bucharest, 1969), p. 129.

[10] F. A. Benson, in *Proceedings of the Fifth International Conference on Ionization Phenomena in Gases, Munich, 1961* (Ref. [9]), p. 235.

[11] K. G. Müller, in *Proceedings of the Fifth International Conference on Ionization Phenomena in Gases, Munich, 1961* (Ref. [9]), p. 253.

[12] G. F. Weston, in *Proceedings of the Fifth International Conference on Ionization Phenomena in Gases, Munich, 1961* (Ref. [9]), p. 528.

[13] G. Ecker, W. Kroll, and O. Zöller, Ann. Phys. (Leipzig) **15**, 60 (1965).

[14] K. G. Emeleus, Int. J. Electron. **42**, 105 (1977).

[15] G. Eckker and K. G. Müller, Institüt für Theoretische Physik der Universität Bonn Technical Report No. FTR (1961) (unpublished), also presented as U.S. Army Report No. DA-91-591-EUC-1254, 1961 (unpublished).

[16] W. Rogowski, Arch. Elektrotech. **20**, 99 (1928); W. Rogowski and A. Wallraff, Z. Phys. **108**, 1 (1938).

[17] R. W. Crowe, J. K. Bragg, and V. G. Thomas, Phys. Rev. **96**, 10 (1954).

[18] D. J. DeBitetto, L. H. Fisher, and A. L. Ward, Phys. Rev. **118**, 920 (1960); A. L. Ward and E. Jones, *ibid.* **122**, 376 (1961).

[19] H. Niesters, in *Proceedings of the Fourth International Conference on Ionization Phenomena in Gases, City, Year* (Ref. [9]), p. 175.

[20] See, for example, E. A. Den Hartog, D. A. Doughty, and J. E. Lawler, Phys. Rev. A **38**, 2471 (1988); A. Mitchell, G. R. Scheller, R. A. Gottscho, and D. B. Graves, *ibid.* **40**, 5199 (1989).

[21] See, for example, the models described by J.-P. Boeuf, in *Physics and Applications of Pseudosparks,* edited by M. A. Gundersen and G. Schaefer (Plenum, New York, 1990), p. 255; T. J. Sommerer, W. N. G. Hitchon, and J. E. Lawler, Phys. Rev. A **39**, 6356 (1989).

[22] See, for example, J. W. Butterbaugh, L. D. Baston, and H. H. Sawin, J. Vac, Sci. Technol. A **8**, 916 (1990); M. A. Lieberman and S. E. Savas, *ibid.* **8**, 1632 (1990).

[23] See, for example, J. Christiansen, in *Physics and Applications of Pseudosparks* (Ref. [21]), p. 1. See also other papers in this conference proceedings.

[24] B. E. Cherrington, *Gaseous Electronics and Gas Lasers* (Pergamon, Oxford, 1979), Chaps. 10–12.

[25] A. V. Phelps, B. M. Jelenković, and L. C. Pitchford, Phys. Rev. A **36**, 5327 (1987).

[26] J. A. Ray, C. F. Barnett, and B. Van Zyl, J. Appl. Phys. **50**, 6516 (1979).

[27] L. B. Loeb, *Fundamental Processes of Electrical Discharges in Gases* (Wiley, New York, 1939), p. 386.

[28] A. V. Phelps, J. Phys. Chem. Ref. Data **20**, 557 (1991). See also A. V. Phelps, *ibid.* **21**, 883 (1992).

[29] Z. Lj. Petrović and A. V. Phelps (unpublished).

[30] The calculated capacitance of the discharge electrodes for the experiments of papers I and II is 40 pF compared to the total circuit and electrode capacitance of 250±10 pF obtained by direct measurement and from the measured postdischarge time constant for voltage decay with a known R_S.

[31] E. Agron, I.-L. Chang, C. Gunaratna, D. K. Kahnaher, and M. A. Reed, IEEE Micro. **8**, 56 (1988).

[32] A. Güntherschulze and S. Schnitger, Z. Phys. **77**, 333 (1932).

[33] G. Ahsmann and H. J. Oskam, J. Appl. Phys. **29**, 1768 (1958).

[34] C. Yeh, J. Appl. Phys. **27**, 98 (1956).

[35] Equation (20) can be used to show that a plot of ω^2 versus I_{SS} should be linear for small ω.

[36] C. G. Morgan, Phys. Rev. **104**, 566 (1956); F. Llewellyn-Jones and E. Jones, Proc. Phys. Soc. **75**, 762 (1960); E. Jones and F. Llewellyn-Jones, *ibid.* **80**, 450 (1962); H. Schlumbohm, Z. Naturforsch. **22a**, 347 (1967).

[37] L. Graf and G. Schmitz, Z. Phys. **170**, 418 (1962); L. Graf, in *Proceedings of the Fifth International Conference on Phenomena in Ionized Gases, Munich, 1961* (Ref. [9]), p. 1585.

[38] A. V. Phelps, J. Phys. Chem. Ref. Data **19**, 653 (1990).

[39] D. E. Davies and R. K. Fitch, Br. J. Appl. Phys. **10**, 502 (1959); G. S. Selwyn, B. D. Ai, and J. Singh, Appl. Phys. Lett. **52**, 1953 (1988).

[40] G. W. McClure and K. D. Granzow, Phys. Rev. **125**, 3 (1962); A. L. Ward, J. Appl. Phys. **33**, 2789 (1962); E. J. Lauer, S. S. Yu, and D. M. Cox, Phys. Rev. A **23**, 2250 (1981); V. S. Boldasov, A. I. Kuz'michev, and D. S. Fillipychev, Izv. Vyash. Uchebn. Zaved. Radiofiz. **27**, 925 (1984) [Sov. Radiophys. **27**, 656 (1984)]; A. C. Dexter, T. Farrel, and M. I. Lees, J. Phys. D **22**, 413 (1989).

[41] A. V. Phelps and B. M. Jelenković, Phys. Rev. A **38**, 2975 (1988).

[42] D. A. Scott and A. V. Phelps, Phys. Rev. A **43**, 3043 (1991); *ibid.* **45**, 4198 (1992) (erratum).

[43] M. A. Folkhard and S. C. Haydon, Aust. J. Phys. **24**, 517, 527 (1971); J. Dutton, J. Phys. Chem. Ref. Data **4**, 577 (1975); Z. Stokic, M. M. F. R. Fraga, J. Bozin, V. Stojanović, Z. Lj. Petrović, and B. M. Jelenković, Phys. Rev. **45**, 7463 (1992).

[44] Z. Lj. Petrović, B. M. Jelenković, and A. V. Phelps, Phys. Rev. Lett. **68**, 325 (1992). For earlier models, see K. D. Granzow and G. W. McClure, Phys. Rev. **125**, 1792 (1962); E. J. Lauer, S. S. Yu, and D. M. Cox, Phys. Rev. A **23**, 2250 (1981).

[45] B. M. Jelenković and A. V. Phelps (unpublished); and in *Proceedings of the Tenth International Conference on Gas Discharges and Their Applications, Swansea, Wales, 1992,* edited by W. T. Williams (University of Swansea, Swansea, Wales, 1992), Vol. II, p. 513.

[46] R. L. Verma, J. Phys. D **10**, 1167 (1977).